



UNIVERSITY OF LEEDS

This is a repository copy of *First-principles calculations of the lattice thermal conductivity of the lower mantle*.

White Rose Research Online URL for this paper:
<http://eprints.whiterose.ac.uk/87481/>

Version: Accepted Version

Article:

Stackhouse, S, Stixrude, L and Karki, BB (2015) First-principles calculations of the lattice thermal conductivity of the lower mantle. *Earth and Planetary Science Letters*, 427. 11 - 17. ISSN 0012-821X

<https://doi.org/10.1016/j.epsl.2015.06.050>

© 2015 Elsevier. This manuscript version is made available under the CC-BY-NC-ND 4.0 license <http://creativecommons.org/licenses/by-nc-nd/4.0/>

Reuse

Unless indicated otherwise, fulltext items are protected by copyright with all rights reserved. The copyright exception in section 29 of the Copyright, Designs and Patents Act 1988 allows the making of a single copy solely for the purpose of non-commercial research or private study within the limits of fair dealing. The publisher or other rights-holder may allow further reproduction and re-use of this version - refer to the White Rose Research Online record for this item. Where records identify the publisher as the copyright holder, users can verify any specific terms of use on the publisher's website.

Takedown

If you consider content in White Rose Research Online to be in breach of UK law, please notify us by emailing eprints@whiterose.ac.uk including the URL of the record and the reason for the withdrawal request.



eprints@whiterose.ac.uk
<https://eprints.whiterose.ac.uk/>

1 **First-principles calculations of the lattice thermal conductivity of the lower mantle**

2 Stephen Stackhouse^{a,*}, Lars Stixrude^b, Bijaya, B. Karki^c

3 ^a *School of Earth and Environment, University of Leeds, Leeds LS2 9JT, United Kingdom.*

4 ^b *Department of Earth Sciences, University College London, Gower Street, London WC1E 6BT, United Kingdom.*

5 ^c *School of Electrical Engineering and Computer Science, Department of Geology and Geophysics, and Center for Computation and
6 Technology, Louisiana State University, Baton Rouge, LA70803, United States of America.*

7
8 *E-mail addresses: s.stackhouse@leeds.ac.uk; l.stixrude@ucl.ac.uk; karki@csc.lsu.edu

9

10

11

12 **Abstract**

13 The temperature variations on top of the core-mantle boundary are governed by the
14 thermal conductivity of the minerals that comprise the overlying mantle. Estimates of the
15 thermal conductivity of the most abundant phase, MgSiO₃ perovskite, at core-mantle
16 boundary conditions vary by a factor of ten. We performed ab initio simulations to
17 determine the lattice thermal conductivity of MgSiO₃ perovskite, finding a value of 6.8 ± 0.9
18 $\text{W m}^{-1} \text{K}^{-1}$ at core-mantle boundary conditions (136 GPa and 4000 K), consistent with
19 geophysical constraints for the thermal state at the base of the mantle. Thermal
20 conductivity depends strongly on pressure, explaining the dynamical stability of super-
21 plumes. The dependence on temperature and composition is weak in the deep mantle: our
22 results exhibit saturation as the phonon mean free path approaches the interatomic
23 spacing. Combining our results with seismic tomography, we find large lateral variations in
24 the heat-flux from the core that have important implications for core dynamics.

25 **Keywords**

26 MgSiO₃ perovskite; thermal conductivity; mantle dynamics

27

28 **1. Introduction**

29 Heat-flux at the core-mantle boundary has important implications for the thermal evolution
30 of the core and mantle (Lay et al., 2008), the size and stability of plumes (Dubuffet et al.,
31 1999), and generation of the magnetic field (Gubbins et al., 2011). Despite this, there is a
32 wide range of estimates of the thermal conductivity of the lower mantle (Osako and Ito,
33 1991; Hofmeister, 2008; Goncharov et al., 2010; de Koker, 2010; Manthilake et al., 2011;
34 Haigis et al., 2012; Ohta et al., 2012; Dekura et al., 2013; Tang et al., 2014; Ammann et
35 al., 2014; Ohta et al., 2014). As insulators and semi-conductors, the major lower mantle
36 phases: (Mg,Fe)SiO₃ perovskite, CaSiO₃ perovskite, and (Mg,Fe)O ferropericlase are
37 expected to conduct heat via phonons (lattice vibrations), but experimental and theoretical
38 studies of their lattice thermal conductivity have suffered significant limitations.

39 Technical constraints mean that experimental measurements are limited to temperature
40 much lower than those in the deep Earth, and thus long extrapolations must be made to
41 estimate values in the lowermost mantle. In addition, while the results of ambient
42 temperature studies of MgSiO₃ perovskite (Osako and Ito, 1991; Ohta et al., 2012) are in
43 reasonable agreement, measurements at elevated temperature (500-1100 K) and 26 GPa
44 (Manthilake et al., 2011), suggests a 300 K lattice thermal conductivity almost twice as
45 large. This suggests that there are discrepancies even at low temperature and pressure.

46 Classical simulations, where simple functional forms define interactions between atoms,
47 also have considerable uncertainties. Haigis et al. (2012) used a classical potential to
48 compute lattice thermal conductivity via equilibrium molecular dynamics and Green-Kubo
49 relations, while Ammann et al. (2014) used a classical potential to calculate lattice thermal
50 conductivity via non-equilibrium molecular dynamics simulations. The difference of up to a
51 factor of two between the studies, for the lattice thermal conductivity of MgSiO₃ perovskite,
52 illustrates the uncertainty due to the choice of classical potential. This source of

53 uncertainty has been highlighted in other studies (Chen et al., 2012; Howell, 2012) and
54 shows the importance of performing ab initio calculations, where forces are calculated
55 from first-principles.

56 Previous ab initio calculations of the lattice thermal conductivity of MgSiO₃ perovskite
57 have also suffered important limitations. Dekura et al. (2013) and Tang et al. (2014)
58 performed lattice dynamics calculations, which are limited by the assumption that
59 anharmonic terms are truncated at third-order. The truncation is significant, because it
60 requires the lattice thermal conductivity to vary as the inverse of the temperature (T^{-1}),
61 more rapidly than observed in silicates and oxide perovskites at temperatures greater than
62 the Debye temperature (Marquardt et al., 2009a; Hofmeister, 2010), and leads to
63 underestimation of the conductivity at high temperature.

64 Here, we take a different approach, calculating the lattice thermal conductivity of MgSiO₃
65 perovskite using the ‘direct’ non-equilibrium molecular dynamics method (NEMD), with
66 forces calculated directly from density functional theory. The direct method, which we have
67 used previously to compute the lattice thermal conductivity of MgO periclase (Stackhouse
68 et al., 2010), has the advantage that anharmonicity is fully included with no truncation. The
69 method is conceptually straightforward: lattice thermal conductivity is calculated from
70 Fourier’s law by computing the temperature gradient induced by an imposed heat-flux.

71 **2. Theory**

72 **2.1 Non-Equilibrium Molecular Dynamics Simulations**

73 The lattice thermal conductivity of MgSiO₃ perovskite was calculated using ab initio non-
74 equilibrium molecular dynamics (Stackhouse and Stixrude, 2010). The method is intuitive,
75 following the design of experimental techniques. The simulation cell is divided up into
76 sections (Fig. 1(a)). One section is designated the ‘hot section’ and another the ‘cold
77 section’. These are separated by a distance of half the length of the simulation cell. At

78 regular intervals heat is transferred from the cold section to the hot section, generating a
79 heat-flux. Over time, a temperature gradient develops between the hot and cold sections
80 (Fig. 1(b)). Once steady state is reached thermal conductivity is calculated from Fourier's
81 law:

$$82 \quad k = - \frac{\langle J(t) \rangle}{\langle dT/dx \rangle} \quad (1)$$

83 where k is the thermal conductivity, and $\langle J(t) \rangle$ and $\langle dT/dx \rangle$ are the time average of the heat-
84 flux and the temperature gradient.

85 In order to conserve the total kinetic energy and linear momentum of the system, the
86 transfer of energy from the cold section to the hot section is achieved by assigning the
87 hottest atom in the cold section and coldest atom in the hot section the velocities that
88 would arise from a hypothetical elastic collision between them (Müller-Plathe, 1997; Nieto-
89 Draghi and Avalos, 2003).

90 The temperature gradient is determined from a linear fit to the temperature of the
91 individual sections. Due to the periodic nature of the simulation, heat enters and leaves
92 from both sides of the hot and cold sections and two temperature gradients develop,
93 leading to a temperature profile resembling that shown in Fig. 1(b). Rather than discard
94 one of them, the temperature of symmetrically equivalent sections is averaged. Due to the
95 non-Newtonian nature of the energy transfer, the temperature gradient is non-linear
96 around the hot and cold sections. In view of this, these sections are excluded from the fit
97 to determine the temperature gradient (Supplementary Material Fig. S1(d)).

98 **2.2 Finite-Size Effects**

99 Our analysis of finite-size effects follows that of Schelling et al. (2002) and has been used
100 widely as a means of obtaining results in the limit of infinite systems (Zhou et al., 2009;

101 Sellan et al., 2010; Howell, 2011a, 2011b, 2012; Hu et al., 2011). Kinetic theory relates
102 thermal conductivity to phonon mean free path

$$103 \quad k = \frac{1}{3} C_v v l \quad (2)$$

104 where C_v is the volumetric heat capacity, v is the mean sound velocity and l is the phonon
105 mean free path. Since phonons are scattered within the hot and cold sections, the longest
106 possible phonon mean free path is equal to the distance between them, i.e. half the length
107 of the simulation cell. If the true phonon mean free path is much longer than this, the
108 thermal conductivity calculated will be significantly underestimated.

109 If we assume that the phonon mean free path is dependent on two independent
110 scattering mechanisms: phonon-phonon scattering and phonon-boundary scattering
111 occurring at the hot and cold sections, then the effective mean free path for a simulation
112 cell of length L is

$$113 \quad l_L^{-1} = l_{ph}^{-1} + l_b^{-1} \quad (3)$$

114 where l_{ph} is the contribution from phonon-phonon scattering and l_b the contribution from
115 phonon-boundary scattering. l_b is assumed to be $L/4$, where L is the total length of the
116 simulation cell. The factor of 4 arises because phonons originating between the hot and
117 cold sections will travel, on average, a quarter of the simulation cell length before
118 encountering the hot and cold sections. Substituting Eq. (3) into (2) and rearranging leads
119 to

$$120 \quad k_L^{-1} = k_\infty^{-1} + bL^{-1} \quad (4)$$

121 where k_L is the thermal conductivity calculated for a simulation cell of length L , k_∞ the
122 thermal conductivity of a simulation cell of infinite length (i.e. the true value) and b a
123 constant equal to

124
$$b = \frac{12}{C_v v} \quad (5)$$

125 Thus by calculating the thermal conductivity for simulation cells of different length and
126 plotting against L^{-1} , one can estimate k_{∞}^{-1} .

127 Previous studies (Sellan et al., 2010; Howell, 2012) have shown that the linear
128 extrapolation (Eq. (4)) may be inaccurate when the phonon mean free path is much longer
129 than the smallest simulation cell. For example, studies of silicon near room temperature,
130 which has a long phonon mean free path, require simulation cells on the order of 10 000
131 atoms. In the case of our calculations, smaller simulation cells are sufficient, since the
132 temperature is much higher and the phonon mean free path much shorter (Tadano et al.,
133 2014). In our previous calculations of periclase (Stackhouse et al., 2010), we used
134 simulation cells of a similar size, and found our results to be in good agreement with other
135 theoretical methods and experimental results, and the phonon mean free path to be
136 shorter than the smallest simulation cell.

137 Phonon mean free paths can be estimated from the slope of the linear relationship
138 between k_L^{-1} and L^{-1} , combining Eqs. (2) and (5)

139
$$l = \frac{bk_{\infty}}{4} \quad (6)$$

140 Estimated values of l (Supplementary Material Table S1) are shorter than the shortest
141 simulation cell used at all temperature and pressures studied, indicating that our
142 simulation cells are large enough to obtain accurate results.

143 Calculations may also be inaccurate if the cross-sectional area of the simulation cell is
144 too small (Schelling et al., 2002; Zhou et al., 2009; Hu et al., 2011). This is because the
145 phonon population is then biased towards those propagating in the long direction of the
146 simulation cell, leading to an overestimate of the thermal conductivity. This is not expected

147 to be a serious issue in our simulations, because the phonon mean free path is
148 comparable to the cross-sectional dimensions. To test this issue, we have performed
149 simulations with different cross-sectional areas at 110 GPa and 1000 K and 110 GPa and
150 3250 K. The results are identical within uncertainty (Supplementary Material Table S1).

151 **3 Calculation Details**

152 Calculations were performed using a version of the density functional theory based VASP
153 code (Kresse and Furthmuller, 1996a, 1996b) modified to perform NEMD. The local
154 density approximation (Perdew and Zunger, 1981) was used for the exchange-correlation
155 functional. Ultrasoft pseudopotentials were employed, with valence electron
156 configurations: $3s^2$ for Mg, $3s^23p^2$ for Si and $2s^22p^4$ for O. The kinetic-energy cut-off for the
157 plane-wave basis set was set to 400 eV and Brillouin zone sampling was restricted to the
158 Γ -point. Fermi-smearing was applied in all calculations, with a broadening-width equal to
159 the simulation temperature. The convergence criteria for the self-consistency loop was 10^{-4}
160 eV. The time-step was set to 1 fs and the Nosé thermostat was employed to maintain a
161 constant temperature (Nosé, 1984). By calculating the forces from first-principles, we
162 avoid issues associated with empirical pair potentials (Chen et al., 2012; Howell, 2012).

163 The dimensions of all simulation cells used in the current work are listed in
164 Supplementary Material Table S2. The cell parameters at each pressure and temperature
165 (P - T) point, were determined from equilibrium molecular dynamics simulations using 80
166 atom MgSiO_3 models.

167 Before each NEMD calculation, the simulation cell was equilibrated by performing 1 ps
168 of equilibrium molecular dynamics, after which energy exchange was initiated. The energy
169 exchange periods used are listed in Supplementary Materials Table S2. These were
170 chosen to produce a temperature difference of 500-1000 K between the hot and cold
171 sections and took values of between 40-80 fs. Simulations using longer exchange periods

172 converged more slowly, and led to values with larger associated uncertainties, because
173 the error in the temperature gradient increased. Initial tests showed that, within a certain
174 range, using different exchange periods had little effect on the results (Supplementary
175 Materials Fig. S2).

176 Most NEMD calculations were run for a minimum of about 50 ps (Supplementary
177 Material Table S2), at least 10 ps of which was allowed for steady state to be reached.
178 Thermal conductivity was calculated using the remaining portion. In general, this led to
179 converged values for the heat-flux, temperature gradient and thermal conductivity
180 (Supplementary Material Fig. S1). When a simulation was judged not to have converged
181 fully i.e. the time average of the thermal conductivity had not have flattened out,
182 simulations were run longer.

183 The uncertainty in the time average of the heat-flux was determined using the
184 appropriate statistics (Flyvbjerg and Petersen, 1989), taking into account correlation. The
185 same method was also used to compute the uncertainty in the time average of the
186 temperature of individual sections. To calculate the temperature gradient the temperatures
187 of symmetrically equivalent sections were averaged and fit using weighted least square
188 regression, but excluding the values for the hot and cold sections and those either side of
189 them (Fig. S1(d)). The thermal conductivity for a simulation cell of infinite length was
190 determined from a weighted least squares fit to a plot of inverse thermal conductivity
191 against inverse simulation cell length (Supplementary Material Figs. S3 and S4). The
192 extrapolated values are listed in Supplementary Material Table S1.

193 **4. Results**

194 At lower mantle conditions, we find that the temperature dependence of the thermal
195 conductivity is weak: at 75 GPa, lattice thermal conductivity decreases from $5.3 \pm 0.7 \text{ Wm}^{-1}\text{K}^{-1}$
196 at 2500 K to 4.7 ± 0.8 at 4000 K (Fig. 2). Note that, our results indicate that the lattice

197 thermal conductivity of MgSiO₃ perovskite is isotropic at 75 GPa and 2500 K to within the
198 uncertainty of our results (Fig. S3 and Table S1), and this is presumed to be the case at all
199 other conditions. All values shown in Figs. 2 and 3 are for the [100] direction. Both here
200 and throughout the manuscript the uncertainties indicate the standard error. This variation
201 is weaker than the often-assumed T^{-1} dependence, and even weaker than the $T^{-2/5}$
202 dependence recently suggested for MgSiO₃ perovskite, based on experimental results at
203 lower pressures and temperatures (Manthilake et al., 2011). Such weak temperature
204 dependence indicates saturation (Roufosse and Klemens, 1974; Marquardt et al., 2009a;
205 Hofmeister, 2010), where the phonon mean free path approaches the inter-atomic
206 spacing. This means that pressure (or density) dependence dominates throughout most of
207 the lower mantle: at 4000 K, lattice thermal conductivity increases from $5.3 \pm 0.7 \text{ Wm}^{-1}\text{K}^{-1}$
208 at 75 GPa to $9 \pm 2 \text{ Wm}^{-1}\text{K}^{-1}$ at 145 GPa (Fig. 2).

209 Our results agree well with room temperature experimental data (Osako and Ito, 1991;
210 Ohta et al., 2012; Ohta et al. 2014), showing comparable pressure dependence. The
211 measurements of Manthilake et al. (2011), show similar temperature dependence, but are
212 higher by about $5 \text{ Wm}^{-1}\text{K}^{-1}$ (Fig. 2 (main)). We note that their results also disagree with the
213 ambient temperature values of Ohta et al. (2012). Lattice dynamics calculations of Dekura
214 et al. (2013) agree with our results at low temperature, as expected, but predict a value
215 half that of our study at core-mantle boundary conditions. We attribute this difference to
216 the truncation of anharmonic terms at third order in the lattice dynamics calculation, which
217 assumes T^{-1} behavior and does not capture the saturation (Roufosse and Klemens, 1974)
218 that we find at high temperature. The values of Tang et al. (2014), which also suffer from
219 truncation of anharmonic terms, are much lower than all other studies. It has been
220 proposed that finite-size effects in NEMD simulations lead to erroneous values (Haigis et
221 al., 2012), but this issue is expected to be minimal for MgSiO₃ perovskite at lower mantle
222 conditions, where the phonon mean free path is short and lattice thermal conductivity is

223 low (Supplementary Material Fig. S4 and Table S1) (Tadano et al., 2014). Indeed,
224 previous simulations based on classical potentials and much larger systems show
225 remarkably similar values of the thermal conductivity at the core-mantle boundary
226 (Ammann et al., 2014).

227 **5. Discussion**

228 Our results serve as a test of approximate theories of the density and temperature
229 dependence of the thermal conductivity. Our results disagree with the commonly assumed
230 T^{-1} or $T^{-1/2}$ temperature dependence. Instead, we find that our results are reproduced well
231 by a model (Supplementary Material Section S1) that combines the Leibfried-Schlömann
232 equation with temperature dependence that includes the effects of saturation (Roufosse
233 and Klemens, 1974)

$$234 \quad k \propto \frac{M\Omega^{1/3}\theta^3}{\gamma^2 T} \left\{ \frac{2}{3} \left[\frac{T_S(\Omega)}{T} \right]^{1/2} + \frac{1}{3} \left[\frac{T}{T_S(\Omega)} \right] \right\} C \quad (7)$$

235 where M is the mean atomic mass, Ω mean atomic volume, θ Debye temperature, γ
236 Grüneisen parameter, T temperature, and $T_S \propto M\Omega^{2/3}\theta^2/\gamma^2$ is the temperature at which
237 saturation becomes significant. The term in the brackets accounts for saturation and
238 causes k to vary more weakly than $T^{-1/2}$ at high temperature, in excellent agreement with
239 our results. The heat capacity C , accounts for phonon population effects at low
240 temperature. All quantities are computed from a thermodynamic model (Stixrude and
241 Lithgow-Bertelloni, 2011). The two constants of proportionality are chosen by fitting to our
242 NEMD results.

243 We estimate the lattice thermal conductivity across the lower mantle, arriving at a value
244 of $8.1 \pm 1.1 \text{ Wm}^{-1}\text{K}^{-1}$ at the core-mantle boundary (Fig. 3), by combining the results of the
245 present work, with our earlier ab initio predictions for periclase (Stackhouse et al., 2010),

246 and scaling laws for minor phases and impurities (Supplementary Material Sections S2 to
247 S4). We approximate the lower mantle as pyrolite: (Mg,Fe)SiO₃ perovskite (75 percent),
248 CaSiO₃ perovskite (6 percent) and (Mg,Fe)O ferropericlasite (19 percent) (Stixrude and
249 Lithgow-Bertelloni, 2011). Recent experimental results show that iron impurities greatly
250 reduce lattice thermal conductivity (Manthilake et al., 2011), at least at the low
251 temperatures at which the measurements were made. By assuming this same large
252 reduction, previous studies (Manthilake et al., 2011; Haigis et al., 2012) arrived at values
253 for the lattice thermal conductivity of the lower mantle similar to ours. However, we expect
254 the impact of impurities to be reduced at lower mantle temperatures. Based on the theory
255 of Klemens (1960), we estimate the fractional lowering of the lattice thermal conductivity of
256 the lower mantle due to iron impurities to be 8 percent at the core-mantle boundary, i.e.
257 our value at the core-mantle boundary in the iron-free limit is very similar: $8.8 \pm 1.2 \text{ Wm}^{-1}\text{K}^{-1}$.
258 The influence of aluminum is expected to be less than that of iron (Ohta et al., 2014).
259 Our value for an iron-free lower mantle is substantially smaller than that estimated in a
260 recent experimental study (Manthilake et al., 2011) which we attribute to the long
261 extrapolation from the experimental results to lower mantle conditions. Our value is a
262 factor of 2 larger than the estimate based on the lattice dynamics calculations of Dekura et
263 al. (2013) and a factor of 6 larger than that based on the lattice dynamics calculations of
264 Tang et al. (2014), which we attribute to the truncation of anharmonic terms in these
265 studies.

266 The thermal conductivity of iron-bearing phases may be influenced by electronic
267 transitions at lower mantle conditions. The influence of the high-spin to low-spin transition
268 on thermal conductivity is unknown. If we assume that the primary effect of the transition is
269 to decrease the atomic spacing, and take the volume decrease of Tsuchiya et al. (2006),
270 based on scaling relations (Supplementary Material Section S2), the lattice thermal
271 conductivity of ferropericlasite may be 3 percent higher in the low-spin state than in the

272 high-spin state. Within the transition region, in which high-spin and low-spin iron coexists
273 in variable amounts, the mean acoustic wave velocity is reduced. If we assume that bulk
274 sound velocity is reduced by the amount reported by Wentzcovitch et al. (2009) and that
275 the shear velocities are unaffected (Marquardt et al., 2009b), based on scaling relations
276 (Supplementary Material Section S2), the lattice thermal conductivity may be 15 percent
277 smaller than the high-spin phase. The influence of the spin transition of the lattice thermal
278 conductivity of perovskite will be much less than in ferropericlase, because of the lower
279 iron content and the smaller fraction of ferrous iron. The spin transition appears to
280 decrease phonon thermal conductivity and reduce the electrical conductivity (Goncharov et
281 al., 2010). Although pure FeO becomes metallic at high pressures and temperatures
282 (Fischer et al., 2011), thermal transport by electrons is unlikely to contribute significantly to
283 thermal conductivity for plausible mantle iron concentrations. Extreme enrichment in iron,
284 i.e. Fe/Si ~ 1 , may produce much greater thermal conductivity by stabilizing new phases in
285 which heat transport by electrons becomes important (Manga and Jeanloz, 1996), but
286 seismic evidence rules out such extreme enrichments, even in ultra-low velocity zones
287 (Rost et al., 2005).

288 In addition to scattering from impurities, scattering from interactions with electrons and
289 grain boundaries can also influence lattice thermal conductivity. In the lower mantle,
290 (Mg,Fe)SiO₃ perovskite, CaSiO₃ perovskite and (Mg,Fe)O ferropericlase are insulators
291 and semiconductors. Older studies of semiconductors (e.g. Boghosian and Dubey, 1978)
292 suggest that phonon-electron scattering is only important at low temperature (< 5 K), but a
293 more recent first-principles investigation (Liao et al., 2015) shows that, for silicon with high
294 carrier concentrations ($> 10^{19}$ cm⁻³), it has a marked effect at room temperature. There are
295 no studies of the effect of phonon-electron scattering at lower mantle conditions, but we
296 note that the analysis of Liao et al. (2015) indicates that phonon-electron scattering is most

297 significant for phonons with a mean free path greater than 100 nm. This is much longer
298 than that expected for phonons in MgSiO₃ perovskite (Supplementary Material Table S1)
299 and MgO periclase (Stackhouse et al. 2010), at lower mantle conditions. Inclusion of
300 impurities will reduce the phonon mean free paths of the phases further. In view of this,
301 we conclude that the effect of phonon-electron scattering is negligible in the lower mantle.

302 The effect of phonon-boundary scattering on lattice thermal conductivity becomes
303 important when the mean free path is comparable to the grain size. Imada et al. (2014)
304 showed that, at 300 K, there is a significant difference between single- and poly-crystal
305 lattice thermal conductivity measurements for MgO periclase, in particular, at high
306 pressure where the phonon mean free path is long in the single-crystal. Their analysis
307 suggests that at core-mantle boundary conditions the lattice thermal conductivity of the
308 phase will be independent of grain size, because of the much shorter mean free path.
309 Since the mean free path of phonons in MgSiO₃ perovskite and iron-bearing phases is
310 expected to be even shorter than that of MgO periclase, the lattice thermal conductivity
311 of the lower mantle should be independent of grain size.

312 In some regions of the lower few hundred kilometers of the mantle, it is expected that
313 perovskite transforms to post-perovskite (Wookey et al., 2005). Some studies indicate that
314 the lattice thermal conductivity of post-perovskite is a factor of two greater than that of
315 perovskite (Ohta et al., 2012; Ammann et al., 2014), but others suggest that this is only
316 true at the low temperatures at which the experiments were conducted and at high
317 temperature the difference is much smaller (Haigis et al., 2012). In view of this, we ignore
318 differences in the lattice thermal conductivities of the two phases. We also neglect
319 possible radiative contributions to the thermal conductivity, because measurements show
320 that these are less than 0.5 Wm⁻¹K⁻¹ (Goncharov et al., 2008). However, we note that a

321 consensus has not yet been reached: another experimental study concludes that the
322 radiative contribution could be up to $5 \text{ Wm}^{-1}\text{K}^{-1}$ (Keppler et al., 2008).

323 Our predicted value of the thermal conductivity at the core-mantle boundary is consistent
324 with a variety of geophysical constraints (Lay et al., 2008). A boundary layer analysis
325 (Supplementary Material Section S4) shows that for a thermal boundary layer thickness δ
326 $\sim 100 \text{ km}$ (Fig. 4), our results satisfy independent constraints on the temperature across
327 the thermal boundary layer from extrapolation of the mantle geotherm and inner-core
328 freezing; the location of the seismic discontinuities caused by the perovskite to post-
329 perovskite phase transition; and bounds on the heat-flow from intra-plate volcanism and
330 heat conducted down the core adiabat.

331 The increase in thermal conductivity with increasing depth (Fig. 3) that we find – nearly a
332 factor of two across the lower mantle – is dynamically significant. Greater thermal
333 conductivity at depth is essential for stabilizing so-called superplumes: large-scale
334 structures in the bottom-most 1000 km of the mantle beneath Africa and the Pacific, with
335 very low shear wave velocity indicating higher than average temperature (Dziewonski et
336 al., 2010). Dynamical simulations (Dubuffet et al., 1999) show that the buoyant instability
337 of hot superplumes can be counter-acted and their long-term stability explained if the
338 thermal conductivity of the lower mantle is higher than the rest of the mantle, just as we
339 find.

340 While the physical model outlined in the previous sections completely specifies the
341 calculation of the lattice thermal conductivity at all pressure and temperature conditions,
342 we recognize that it may be useful to have a simpler, approximate form that captures the
343 essence of these results. We present a simple approximation to the variation of the lattice
344 thermal conductivity of pyrolite with pressure and temperature that is valid across the
345 lower mantle regime

346
$$k = (4.9 \text{ GPa} + 0.105P)f\left(\frac{T}{1200\text{K}}\right)\left(\frac{1200\text{K}}{T}\right) \quad (8)$$

347 where k is thermal conductivity ($\text{Wm}^{-1}\text{K}^{-1}$), P is pressure (GPa), T is temperature (K) and f
348 is a function based on the theory of Roufosse and Klemens (1974), which accounts for
349 saturation (Supplementary Material Section S1). This equation reproduces our results for
350 pyrolite to within 10 percent along mantle geotherms with potential temperatures between
351 1000 K and 2000 K and with or without a bottom thermal boundary layer and over the
352 entire lower mantle pressure regime.

353 According to our results the thermal conductivity in the lower mantle is nearly
354 homogeneous laterally, because of the weak dependence that we find on temperature and
355 impurities. For example, varying the temperature by ± 500 K, changes the thermal
356 conductivity at the core-mantle boundary by only 5 percent. Superplumes may also be
357 stabilized by chemical heterogeneity; indeed seismic evidence of sharp sides indicates
358 that they have a different chemical composition from normal mantle (Ni et al., 2002). We
359 find that, in the lower mantle, the influence of chemical heterogeneity on thermal
360 conductivity is minor (e.g. doubling the Fe/Mg ratio decreases the conductivity by only 5
361 percent). This idea was also suggested by Manthilake et al. (2011), who showed that iron
362 concentration has little effect on the lattice thermal conductivity of (Mg,Fe)O ferropericlase,
363 although we note that they estimate a much larger difference between an iron-free and
364 iron-bearing lower mantle (50 percent) than that found in this study (8 percent). It was
365 suggested by Ohta et al. (2012), that the difference between iron-free and iron-bearing
366 phases observed in lower pressure measurements (< 26 GPa) by Manthilake et al. (2011)
367 should be diminished at lower mantle pressures where iron will exist in a low-spin state.
368 Enrichment in aluminum is expected to have a smaller effect, because of the similarity in
369 atomic mass of aluminum to magnesium and silicon. This assumption is supported by
370 the results of Ohta et al. (2014), but conflicts with those of Manthilake et al. (2011).

371 Lateral homogeneity in thermal conductivity at the core-mantle boundary is significant,
372 because it implies a direct relationship between the temperature in the lower-most mantle,
373 which can be inferred from seismology (Kustowski et al., 2008), and lateral variations in
374 the heat-flux across the core-mantle boundary, via Fourier's law (Nakagawa and Tackley,
375 2008). Combining Fourier's law for the heat-flux $q = k\partial T/\partial z$, with a linear temperature
376 profile near the core-mantle boundary $T = T_{CMB} - h\partial T/\partial z$, and scaling of shear-wave velocity
377 to temperature $\xi = (\partial \ln V_S/\partial T)_z$ we find lateral variations in the heat-flux $dq = -k/h \, d \ln V_S/\xi$,
378 where T is temperature, z is depth, T_{CMB} is the temperature at the core-mantle boundary, h
379 is height above the core-mantle boundary, and V_S is shear-wave velocity. To compute dq
380 we use our value of k for pyrolite at the core-mantle boundary, $d \ln V_S$ from seismic
381 tomography at 2800 km depth, giving $h = 90$ km, and the scaling ξ from a thermodynamic
382 model (Stixrude and Lithgow-Bertelloni, 2011). We do not include the influence of the
383 perovskite to post-perovskite transition on ξ because the pressure at which the transition
384 occurs is uncertain. We find substantial lateral variation in heat-flux, comparable in
385 magnitude to the mean value (Fig. 5). The heat-flux varies from zero (i.e. no heat escaping
386 the core) to nearly twice the mean value. Such large lateral variations in heat-flux have
387 important implications for our understanding of the origin of Earth's magnetic field (Olson
388 and Christensen, 2002), its behaviour during reversals (Glatzmaier et al., 1999), and the
389 structure of the inner core (Gubbins et al., 2011). Geodynamo simulations (Gubbins et al.,
390 2011) indicate that even for much smaller lateral variation in heat flow than we estimate,
391 localized melting of the inner core may occur, which may help to explain anomalies in the
392 structure of the inner core including its radial structure, anisotropy, and hemispherical
393 dichotomy. We note that our estimates of the lateral variation of heat flux are based on the
394 assumption that lateral variations in seismic wave velocity are purely thermal in origin. An

395 understanding of the contributions of lateral variations in chemistry to the tomographic
396 signal will be important for understanding the pattern of heat flow.

397 **6. Conclusions**

398 In conclusion, our calculations suggest that the lattice thermal conductivity of MgSiO_3
399 perovskite depends strongly on pressure, but that temperature and compositional
400 dependence is weak in the deep mantle. Combining our results with seismic tomography,
401 we find large lateral variations in the heat-flux from the core that have important
402 implications for core dynamics. Our predictions of the thermal conductivity provide a firm
403 basis from which further to explore the influence of mantle chemical heterogeneity on the
404 coupled thermal evolution of core and mantle.

405

406

407 **Acknowledgements**

408 This research was supported by the European Research Council under Advanced Grant
409 No. 291432 “MoltenEarth” (FP7/2007-2013), NERC grant number NE/K006290/1 and the
410 National Science Foundation through TeraGrid resources provided by the Texas
411 Advanced Computing Center, under NSF grant EAR080017. In addition, we also
412 acknowledge the use of high performance computing provided by Advanced Research
413 Computing at the University of Leeds and HECToR, the UK's national high-performance
414 computing service, which is provided by UoE HPCx Ltd at the University of Edinburgh,
415 Cray Inc and NAG Ltd, and funded by the Office of Science and Technology through
416 EPSRC's High End Computing Programme. The authors thank Carolina Lithgow-Bertelloni
417 for assistance preparing Fig. 5, and the editor and two anonymous reviewers for
418 constructive comments. S.S. thanks Michael Ammann, John Brodholt, David Dobson, and
419 Andrew Walker for useful discussions.

420

421 **Appendix A. Supplementary Material**

422 Supplementary material related to this article can be found online.

423

424

425

426

427 **References**

- 428 Ammann, M.W., Walker, A.M., Stackhouse, S., Wookey, J., Forte, A.M., Brodholt, J.P.,
429 Dobson, D.P., 2014. Variation of thermal conductivity and heat flux at the Earth's
430 core mantle boundary. *Earth Planet. Sci. Lett.* 390, 175–185.
- 431 Boghosian, H.H., Dubey, K.S., 1978. Role of Electron-Phonon Interaction and Peripheral
432 Phonons in the Lattice Thermal Conductivity of Doped Semiconductor at Low
433 Temperatures. *Phys. Stat. Sol.* 88, 417-427.
- 434 Chen, Y., Chernatynskiy, A., Brown, D., Schelling, P.K., Artacho, E., Phillpot, S.R., 2012.
435 Critical assessment of classical potentials for MgSiO₃ perovskite with application to
436 thermal conductivity. *Phys. Earth Planet. Inter.* 210-211, 75–89.
- 437 Davies, G.F., 2007. Mantle regulation of core cooling: A geodynamo without core
438 radioactivity? *Phys. Earth Planet. Inter.* 160, 215–229.
- 439 de Koker, N., 2010. Thermal conductivity of MgO periclase at high pressure: Implications
440 for the D'' region. *Earth Planet. Sci. Lett.* 292, 392–398.
- 441 Dekura, H., Tsuchiya, T., Tsuchiya, J., 2013. Ab initio Lattice Thermal Conductivity of
442 MgSiO₃ Perovskite as Found in Earth's Lower Mantle. *Phys. Rev. Lett.* 110,
443 025904.
- 444 Dubuffet, F., Yuen, D.A., Rabinowicz, M., 1999. Effects of a realistic mantle thermal
445 conductivity on the patterns of 3-D convection. *Earth Planet. Sci. Lett.* 171, 401–
446 409.
- 447 Dziewonski, A.M., Lekic, V., Romanowicz, B.A., 2010. Mantle Anchor Structure: An
448 argument for bottom up tectonics. *Earth Planet. Sci. Lett.* 299, 69–79.
- 449 Fischer, R.A., Campbell, A.J., Lord, O.T., Shofner, G.A., Dera, P., Prakapenka, V.B.,
450 2011. Phase transition and metallization of FeO at high pressures and
451 temperatures. *Geophys. Res. Lett.* 38, L24301.

453 Flyvbjerg, H., Petersen, H., 1989. Error-estimates on averages of correlated data. J.
454 Chem. Phys. 91, 461–466.

455 Glatzmaier, G.A., Coe, R.S., Hongre, L., Roberts, P.H., 1999. The role of the Earth's
456 mantle in controlling the frequency of geomagnetic reversals. Nature 401, 885–890.

457 Goncharov, A.F., Haugen, B.D., Struzhkin, V.V., Beck, P., Jacobsen, S.D., 2008.
458 Radiative conductivity in the Earth's lower mantle. Nature 456, 231–234.

459 Goncharov, A.F., Struzhkin, V.V., Montoya, J.A., Kharlamova, S., Kundargi, R., Siebert, J.,
460 Badro, J., Antonangeli, D., Ryerson, F.J., Mao, W., 2010. Effect of composition,
461 structure, and spin state on the thermal conductivity of the Earth's lower mantle.
462 Phys. Earth Planet. Inter. 180, 148–153.

463 Gubbins, D., Sreenivasan, B., Mound, J., Rost, S., 2011. Melting of the Earth's inner core.
464 Nature 473, 361–U53.

465 Haigis, V., Salanne, M., Jahn, S., 2012. Thermal conductivity of MgO, MgSiO₃ perovskite
466 and post-perovskite in the Earth's deep mantle. Earth Planet. Sci. Lett. 355-356,
467 102–108.

468 Hofmeister, A.M., 2008. Inference of high thermal transport in the lower mantle from laser-
469 flash experiments and the damped harmonic oscillator model. Phys. Earth Planet.
470 Inter. 170, 201–206.

471 Hofmeister, A.M., 2010. Thermal diffusivity of oxide perovskite compounds at elevated
472 temperature. J. Appl. Phys. 107, 103532.

473 Howell, P.C., 2011a. Thermal Conductivity Calculation with the Molecular Dynamics Direct
474 Method II: Improving the Computational Efficiency. J. Comput. Theor. Nanosci. 8,
475 2144–2154.

476 Howell, P.C., 2011b. Thermal Conductivity Calculation with the Molecular Dynamics Direct
477 Method I: More Robust Simulations of Solid Materials. J. Comput. Theor. Nanosci.
478 8, 2129–2143.

479 Howell, P.C., 2012. Comparison of molecular dynamics methods and interatomic
480 potentials for calculating the thermal conductivity of silicon. *J. Chem. Phys.* 137,
481 224111.

482 Hu, L., Evans, W.J., Koblinski, P., 2011. One-dimensional phonon effects in direct
483 molecular dynamics method for thermal conductivity determination. *J. Appl. Phys.*
484 110, 113511.

485 Imada, S., Ohta, K., Yagi, T., Hirose, K., Yoshida, H., Nagahara, H., 2014. Measurements
486 of lattice thermal conductivity of MgO to core-mantle boundary pressures. *Geophys.*
487 *Rev. Lett.* 41, 060423.

488 Keppler, H., Dubrovinsky, L.S., Narygina, O., Kantor, I., 2008. Optical Absorption and
489 Radiative Thermal Conductivity of Silicate Perovskite to 125 Gigapascals. *Science*
490 322, 1529–1532.

491 Klemens, P., 1960. Thermal resistance due to point defects at high temperatures. *Phys.*
492 *Rev.* 119, 507–509.

493 Kresse, G., Furthmuller, J., 1996a. Efficiency of ab-initio total energy calculations for
494 metals and semiconductors using a plane-wave basis set. *Comput. Mater. Sci.* 6,
495 15–50.

496 Kresse, G., Furthmuller, J., 1996b. Efficient iterative schemes for ab initio total-energy
497 calculations using a plane-wave basis set. *Phys. Rev. B* 54, 11169–11186.

498 Kustowski, B., Ekstrom, G., Dziewonski, A.M., 2008. Anisotropic shear-wave velocity
499 structure of the Earth's mantle: A global model. *J. Geophys. Res.-Solid Earth* 113,
500 B06306.

501 Lay, T., Hernlund, J., Buffett, B.A., 2008. Core-mantle boundary heat flow. *Nat. Geosci.* 1,
502 25–32.

503 Liao, B., Qiu, B., Zhou, J., Huberman, S., Esfarjani, K., Chen, G., 2015. Significant
504 Reduction of Lattice Thermal Conductivity by the Electron-Phonon Interaction in

505 Silicon with High Carrier Concentrations: A First-Principles Study. *Phys. Rev. Lett.*
506 114, 115901.

507 Manga, M., Jeanloz, R., 1996. Implications of a metal-bearing chemical boundary layer in
508 D'' for mantle dynamics. *Geophys. Res. Lett.* 23, 3091–3094.

509 Manthilake, G.M., de Koker, N., Frost, D.J., McCammon, C.A., 2011. Lattice thermal
510 conductivity of lower mantle minerals and heat flux from Earth's core. *Proc. Natl.*
511 *Acad. Sci. U. S. A.* 108, 17901–17904.

512 Marquardt, H., Ganschow, S., Schilling, F.R., 2009a. Thermal diffusivity of natural and
513 synthetic garnet solid solution series. *Phys. Chem. Miner.* 36, 107–118.

514 Marquardt, H., Speziale, S., Reichmann, H.J., Frost, D.J., Schilling, F.R. 2009b. Single-
515 crystal elasticity of (Mg_{0.9},Fe_{0.1})O to 81 GPa. *Earth. Planet. Sci. Lett.* 3-4, 345–352.

516 Muller-Plathe, F., 1997. A simple nonequilibrium molecular dynamics method for
517 calculating the thermal conductivity. *J. Chem. Phys.* 106, 6082–6085.

518 Nakagawa, T., Tackley, P.J., 2008. Lateral variations in CMB heat flux and deep mantle
519 seismic velocity caused by a thermal-chemical-phase boundary layer in 3D
520 spherical convection. *Earth Planet. Sci. Lett.* 271, 348–358.

521 Ni, S.D., Tan, E., Gurnis, M., Helmberger, D., 2002. Sharp sides to the African
522 superplume. *Science* 296, 1850–1852.

523 Nieto-Draghi, C., Avalos, J.B., 2003. Non-equilibrium momentum exchange algorithm for
524 molecular dynamics simulation of heat flow in multicomponent systems. *Mol.*
525 *Phys.* 101, 2303–2307.

526 Nose, S., 1984. A unified formulation of the constant temperature molecular dynamics
527 methods. *J. Chem. Phys.* 81, 511–519.

528 Ohta, K., Yagi, T., Hirose, K., 2014. Thermal diffusivities of MgSiO₃ and Al-bearing
529 MgSiO₃ perovskites. *Am. Miner.* 99, 94–97.

530 Ohta, K., Yagi, T., Taketoshi, N., Hirose, K., Komabayashi, T., Baba, T., Ohishi, Y.,
531 Hernlund, J., 2012. Lattice thermal conductivity of MgSiO₃ perovskite and post-
532 perovskite at the core-mantle boundary. *Earth Planet. Sci. Lett.* 349-350, 109–115.

533 Olson, P., Christensen, U.R., 2002. The time-averaged magnetic field in numerical
534 dynamos with non-uniform boundary heat flow. *Geophys. J. Int.* 151, 809–823.

535 Osako, M., Ito, E., 1991. Thermal-diffusivity of MgSiO₃ perovskite. *Geophys. Res. Lett.* 18,
536 239–242.

537 Perdew, J., Zunger, A., 1981. Self-interaction correction to density-functional
538 approximations for many-electron systems. *Phys. Rev. B* 23, 5048–5079.

539 Rost, S., Garnero, E.J., Williams, Q., Manga, M., 2005. Seismological constraints on a
540 possible plume root at the core-mantle boundary. *Nature* 435, 666–669.

541 Roufosse, M., Klemens, P., 1973. Thermal-conductivity of complex dielectric crystals.
542 *Phys. Rev. B* 7, 5379–5386.

543 Roufosse, M., Klemens, P., 1974. Lattice thermal-conductivity of minerals at high-
544 temperatures. *J. Geophys. Res.* 79, 703–705.

545 Schelling, P.K., Phillpot, S.R., Keblinski, P., 2002. Comparison of atomic-level simulation
546 methods for computing thermal conductivity. *Phys. Rev. B* 65.

547 Sellan, D.P., Landry, E.S., Turney, J.E., McGaughey, A.J.H., Amon, C.H., 2010. Size
548 effects in molecular dynamics thermal conductivity predictions. *Phys. Rev. B* 81.

549 Stackhouse, S., Stixrude, L., 2010. Theoretical Methods for Calculating the Lattice
550 Thermal Conductivity of Minerals, in: Wentzcovitch, R., Stixrude, L. (Eds.),
551 Theoretical and Computational Methods in Mineral Physics: Geophysical
552 Applications. Mineralogical Soc. Amer., Chantilly, pp. 253–269.

553 Stackhouse, S., Stixrude, L., Karki, B.B., 2010. Thermal Conductivity of Periclase (MgO)
554 from First Principles. *Phys. Rev. Lett.* 104.

555 Stixrude, L., Lithgow-Bertelloni, C., 2011. Thermodynamics of mantle minerals - II. Phase
556 equilibria. *Geophys. J. Int.* 184, 1180–1213.

557 Tadano, T., Gohda, Y., Tsuneyuki, S., 2014. Anharmonic force constants extracted from
558 first-principles molecular dynamics: applications to heat transfer simulations. *J.*
559 *Phys.-Condes. Matter* 26, 225402.

560 Tang, X., Ntam, M.C., Dong, J., Rainey, E.S.G., Kavner, A., 2014. The thermal
561 conductivity of Earth's lower mantle. *Geophysical Research Letters* 41, 2746–2752.

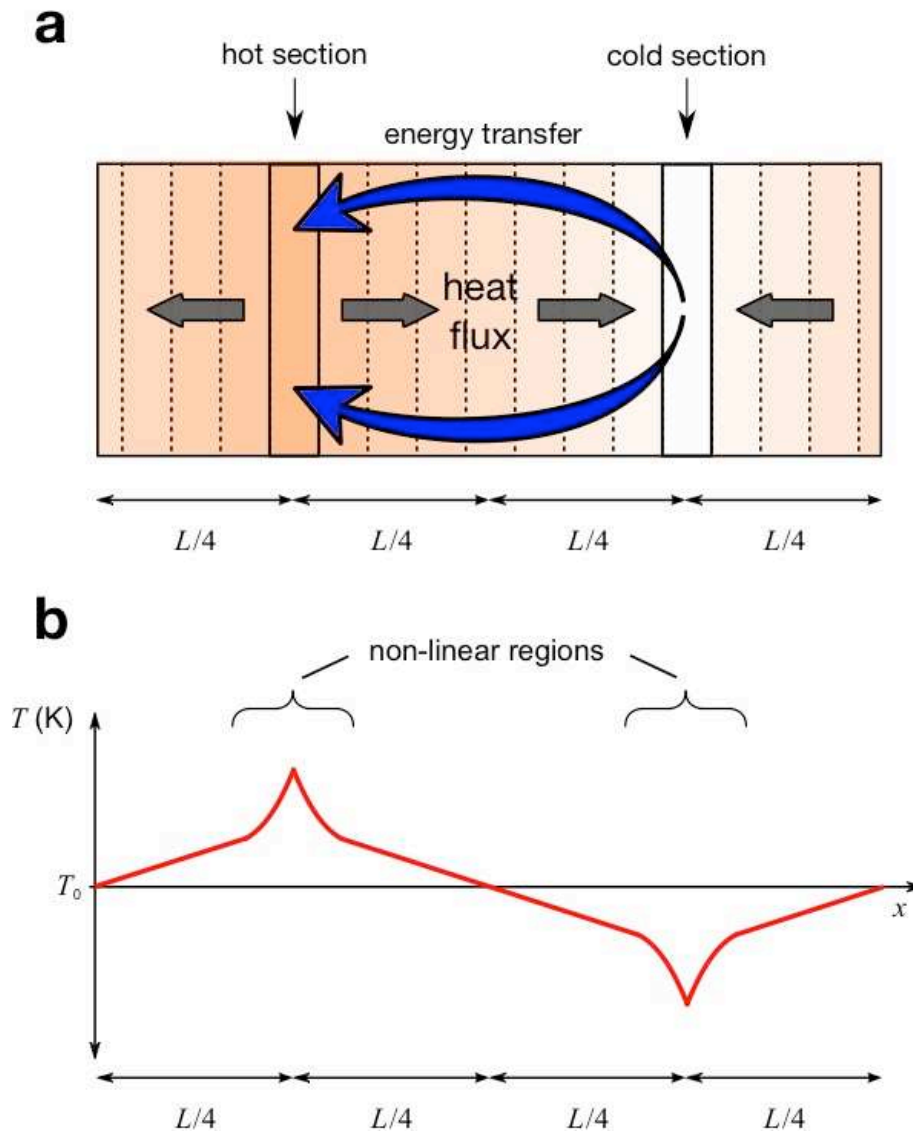
562 Tsuchiya, T., Wentzcovitch, R.M., da Silva, C.R.S., de Gironcoli, S., 2006. Spin transition
563 in magnesiowustite in earth's lower mantle. *Phys. Rev. Lett.* 96.

564 Wentzcovitch, R.M., Justo, J.F., Wu, Z., da Silva, C.R.S., Yuen, D.A., Kohlstedt, D., 2009.
565 Anomalous compressibility of ferropericlase throughout the iron spin cross-over.
566 *Proc. Natl. Acad. Sci. U. S. A.* 106, 8447–8452.

567 Wookey, J., Stackhouse, S., Kendall, J.M., Brodholt, J., Price, G.D., 2005. Efficacy of the
568 post-perovskite phase as an explanation for lowermost-mantle seismic properties.
569 *Nature* 438, 1004–1007.

570 Zhou, X.W., Aubry, S., Jones, R.E., Greenstein, A., Schelling, P.K., 2009. Towards more
571 accurate molecular dynamics calculation of thermal conductivity: Case study of
572 GaN bulk crystals. *Phys. Rev. B* 79.

573

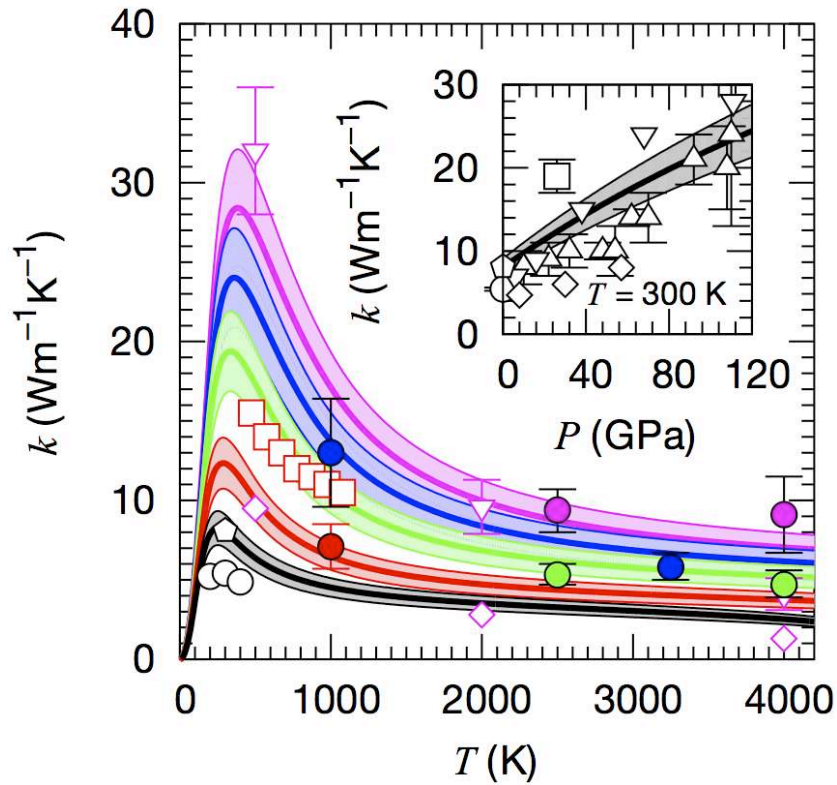


575
576
577

Fig. 1. The non-equilibrium molecular dynamics method for calculating lattice thermal conductivity. The simulation cell is split into sections of equal width. At regular intervals energy is transferred from the 'cold section' to the 'hot section', by means of a virtual elastic collision between the hottest atom in the cold section and coldest atom in the hot section. Due to the periodic nature of the simulation, two temperature gradients form. The non-Newtonian nature of the virtual elastic collision means that the temperature gradient is non-linear around the hot and cold sections. Figure after Stackhouse and Stixrude (2010).

584

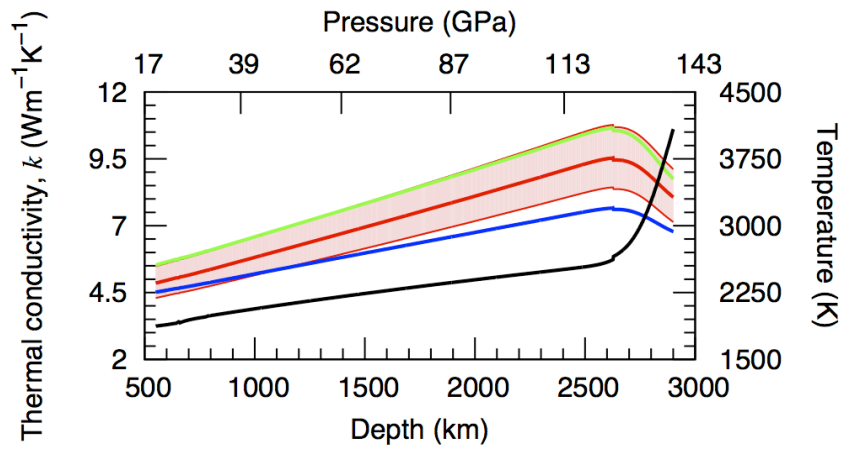
585



586

587 **Fig. 2.** Lattice thermal conductivity of MgSiO_3 perovskite as a function of temperature at
 588 various pressures (main) and a function of pressure at 300 K (inset). Filled circles are the
 589 results of our NEMD simulations and lines are the values predicted by our model
 590 (described in the main text), with shading and error bars indicating standard error. Empty
 591 symbols are measured (\circ Osako and Ito (1991), \square Manthilake et al. (2011), \triangle Ohta et al.
 592 (2012), \pentagon Ohta et al. (2014)) and calculated (∇ Dekura et al. (2013), \diamond Tang et al.
 593 (2014)) values from previous studies. Color code for the main figure: black: 0 GPa, red:26
 594 GPa, green:75 GPa, blue:110 GPa and pink:145 GPa.

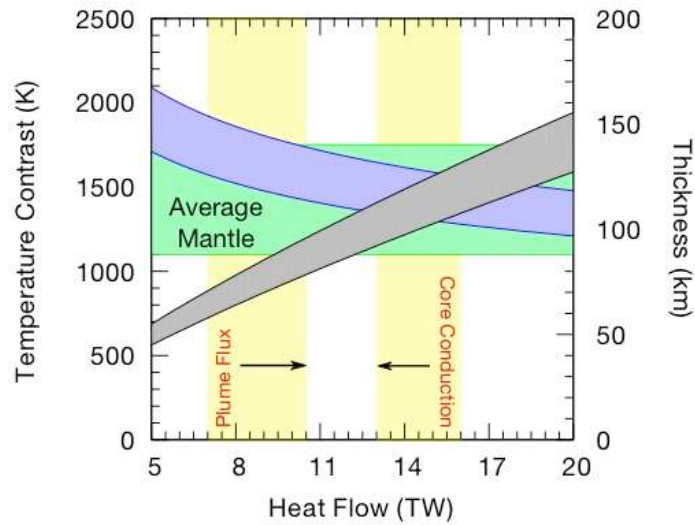
595



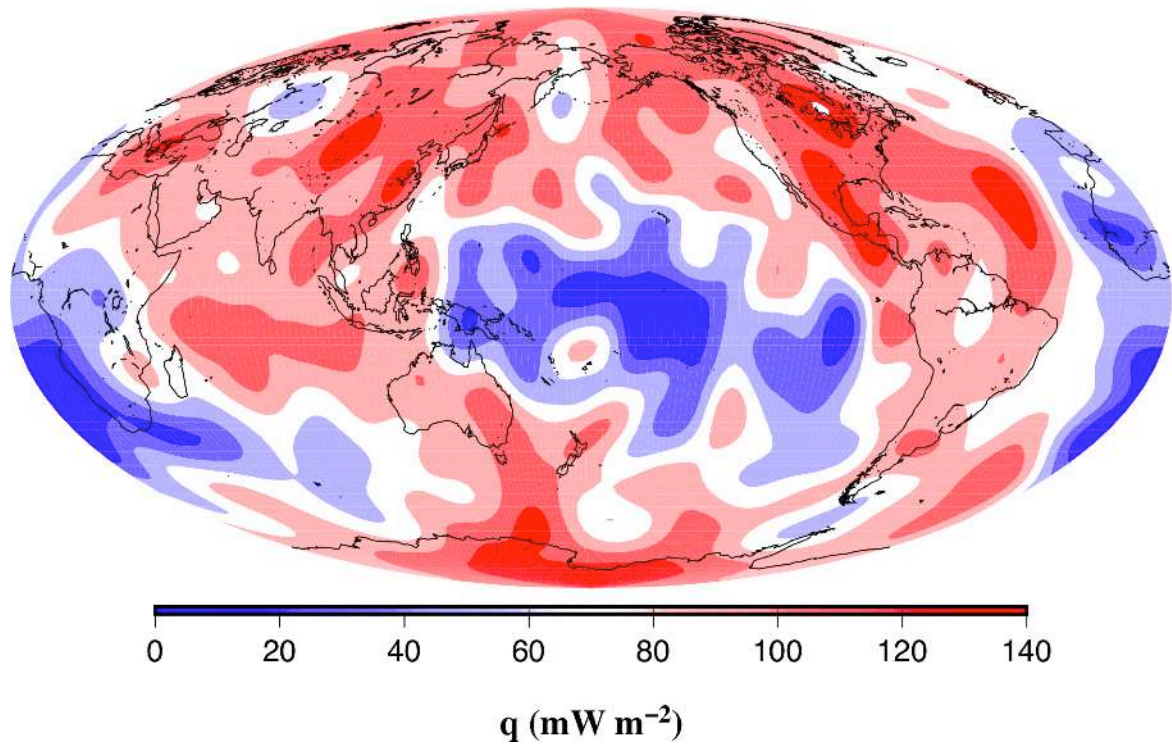
597

598 **Fig. 3.** Lattice thermal conductivity of a pyrolite mantle as a function of depth (red line, with
 599 the shading indicating standard error). Our results for pure MgSiO₃ perovskite (blue line)
 600 and iron-free pyrolite (green line) are shown for comparison. The geotherm (black line) is
 601 taken from a thermodynamic model (Stixrude and Lithgow-Bertelloni, 2011).

602



603
 604 **Fig. 4.** Boundary layer analysis of heat flow. Temperature contrast ΔT (grey band) and
 605 thickness δ (blue band) of the thermal boundary layer plotted against core-mantle
 606 boundary heat flow, with the shading indicating the standard error in our determination of
 607 the thermal conductivity (Supplementary Material Section S4). The green shaded area
 608 denotes constraints on the temperature contrast across the core-mantle boundary. The
 609 orange regions highlight constraints on the heat flow at the core-mantle boundary: upper
 610 bound derived from the heat conducted down the core adiabat and lower bound derived
 611 from the plume heat-flux and the factor 2-3 increase in the plume thermal anomaly with
 612 depth (Davies, 2007).
 613



614
615

616 **Fig. 5.** Heat-flow at the core-mantle boundary. Values calculated from our estimate of
617 thermal conductivity and the seismic tomographic model of Kustowski et al. (2008) at 2800
618 km depth.

619